7
FLOW PATTERNS

7.1 INTRODUCTION

From a practical engineering point of view one of the major design difficulties in dealing with multiphase flow is that the mass, momentum, and energy transfer rates and processes can be quite sensitive to the geometric distribution or topology of the components within the flow. For example, the geometry may strongly effect the interfacial area available for mass, momentum or energy exchange between the phases. Moreover, the flow within each phase or component will clearly depend on that geometric distribution. Thus we recognize that there is a complicated two-way coupling between the flow in each of the phases or components and the geometry of the flow (as well as the rates of change of that geometry). The complexity of this two-way coupling presents a major challenge in the study of multiphase flows and there is much that remains to be done before even a superficial understanding is achieved.

An appropriate starting point is a phenomenological description of the geometric distributions or *flow patterns* that are observed in common multiphase flows. This chapter describes the flow patterns observed in horizontal and vertical pipes and identifies a number of the instabilities that lead to transition from one flow pattern to another.

7.2 TOPOLOGIES OF MULTIPHASE FLOW

7.2.1 Multiphase flow patterns

A particular type of geometric distribution of the components is called a *flow pattern* or *flow regime* and many of the names given to these flow patterns (such as annular flow or bubbly flow) are now quite standard. Usually the flow patterns are recognized by visual inspection, though other means such

as analysis of the spectral content of the unsteady pressures or the fluctuations in the volume fraction have been devised for those circumstances in which visual information is difficult to obtain (Jones and Zuber, 1974).

For some of the simpler flows, such as those in vertical or horizontal pipes, a substantial number of investigations have been conducted to determine the dependence of the flow pattern on component volume fluxes, (j_A, j_B), on volume fraction and on the fluid properties such as density, viscosity, and surface tension. The results are often displayed in the form of a *flow regime map* that identifies the flow patterns occurring in various parts of a parameter space defined by the component flow rates. The flow rates used may be the volume fluxes, mass fluxes, momentum fluxes, or other similar quantities depending on the author. Perhaps the most widely used of these flow pattern maps is that for horizontal gas/liquid flow constructed by Baker (1954). Summaries of these flow pattern studies and the various empirical laws extracted from them are a common feature in reviews of multiphase flow (see, for example, Wallis 1969 or Weisman 1983).

The boundaries between the various flow patterns in a flow pattern map occur because a regime becomes unstable as the boundary is approached and growth of this instability causes transition to another flow pattern. Like the laminar-to-turbulent transition in single phase flow, these multiphase transitions can be rather unpredictable since they may depend on otherwise minor features of the flow, such as the roughness of the walls or the entrance conditions. Hence, the flow pattern boundaries are not distinctive lines but more poorly defined transition zones.

But there are other serious difficulties with most of the existing literature on flow pattern maps. One of the basic fluid mechanical problems is that these maps are often dimensional and therefore apply only to the specific pipe sizes and fluids employed by the investigator. A number of investigators (for example Baker 1954, Schicht 1969 or Weisman and Kang 1981) have attempted to find generalized coordinates that would allow the map to cover different fluids and pipes of different sizes. However, such generalizations can only have limited value because several transitions are represented in most flow pattern maps and the corresponding instabilities are governed by different sets of fluid properties. For example, one transition might occur at a critical Weber number, whereas another boundary may be characterized by a particular Reynolds number. Hence, even for the simplest duct geometries, there exist no universal, dimensionless flow pattern maps that incorporate the full, parametric dependence of the boundaries on the fluid characteristics.

Beyond these difficulties there are a number of other troublesome questions. In single phase flow it is well established that an entrance length of 30 to 50 diameters is necessary to establish fully developed turbulent pipe flow. The corresponding entrance lengths for multiphase flow patterns are less well established and it is quite possible that some of the reported experimental observations are for temporary or developing flow patterns. Moreover, the implicit assumption is often made that there exists a unique flow pattern for given fluids with given flow rates. It is by no means certain that this is the case. Indeed, in chapter 16, we shall see that even very simple models of multiphase flow can lead to conjugate states. Consequently, there may be several possible flow patterns whose occurence may depend on the initial conditions, specifically on the manner in which the multiphase flow is generated.

In summary, there remain many challenges associated with a fundamental understanding of flow patterns in multiphase flow and considerable research is necessary before reliable design tools become available. In this chapter we shall concentrate on some of the qualitative features of the boundaries between flow patterns and on the underlying instabilities that give rise to those transitions.

7.2.2 Examples of flow regime maps

Despite the issues and reservations discussed in the preceding section it is useful to provide some examples of flow regime maps along with the definitions that help distinguish the various regimes. We choose to select the first examples from the flows of mixtures of gas and liquid in horizontal and vertical tubes, mostly because these flows are of considerable industrial interest. However, many other types of flow regime maps could be used as examples and some appear elsewhere in this book; examples are the flow regimes described in the next section and those for granular flows indicated in figure 13.5.

We begin with gas/liquid flows in horizontal pipes (see, for example, Hubbard and Dukler 1966, Wallis 1969, Weisman 1983). Figure 7.1 shows the occurence of different flow regimes for the flow of an air/water mixture in a horizontal, $5.1cm$ diameter pipe where the regimes are distinguished visually using the definitions in figure 7.2. The experimentally observed transition regions are shown by the hatched areas in figure 7.1. The solid lines represent theoretical predictions some of which are discussed later in this chapter. Note that in a mass flux map like this the ratio of the ordinate to the abscissa is $\mathcal{X}/(1-\mathcal{X})$ and therefore the mass quality, $\mathcal{X}$, is known at every point in

the map. There are many industrial processes in which the mass quality is a key flow parameter and therefore mass flux maps are often preferred.

Other examples of flow regime maps for horizontal air/water flow (by different investigators) are shown in figures 7.3 and 7.4. These maps plot the volumetric fluxes rather than the mass fluxes but since the densities of the liquid and gas in these experiments are relatively constant, there is a rough equivalence. Note that in a volumetric flux map the ratio of the ordinate to the abscissa is $\beta/(1-\beta)$and therefore the volumetric quality, β, is known at every point in the map.

Figure 7.4 shows how the boundaries were observed to change with pipe diameter. Moreover, figures 7.1 and 7.4 appear to correspond fairly closely. Note that both show well-mixed regimes occuring above some critical liquid flux and above some critical gas flux; we expand further on this in section 7.3.1.

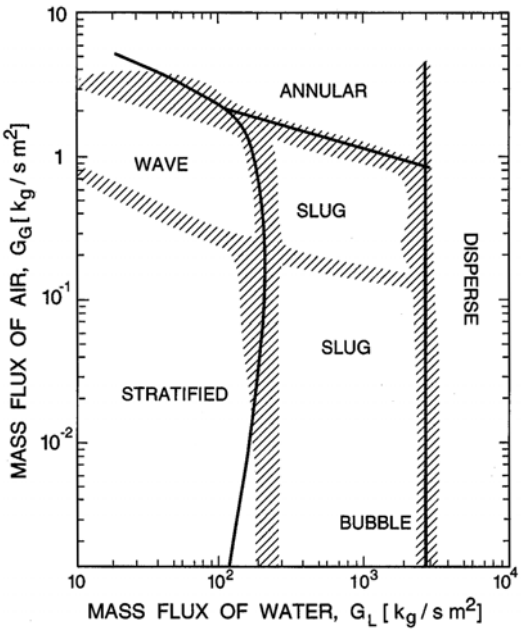

Figure 7.1. Flow regime map for the horizontal flow of an air/water mixture in a $5.1cm$ diameter pipe with flow regimes as defined in figure 7.2. Hatched regions are observed regime boundaries, lines are theoretical predictions. Adapted from Weisman (1983).

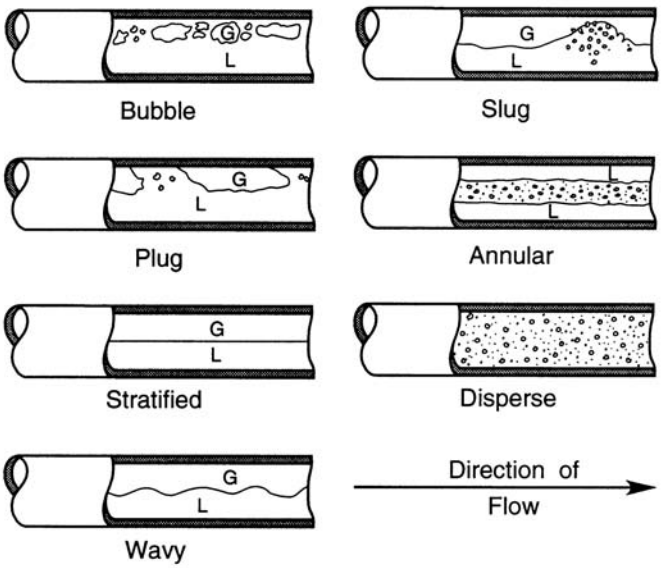

Figure 7.2. Sketches of flow regimes for flow of air/water mixtures in a horizontal, $5.1cm$ diameter pipe. Adapted from Weisman (1983).

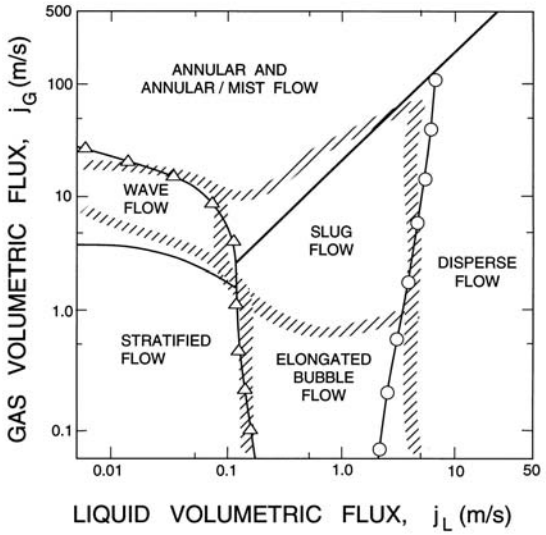

Figure 7.3. A flow regime map for the flow of an air/water mixture in a horizontal, $2.5cm$ diameter pipe at $25°C$ and $1bar$. Solid lines and points are experimental observations of the transition conditions while the hatched zones represent theoretical predictions. From Mandhane *et al.* (1974).

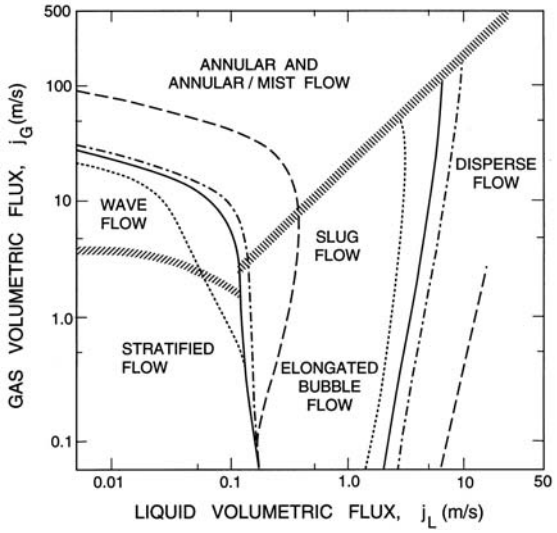

Figure 7.4. Same as figure 7.3 but showing changes in the flow regime boundaries for various pipe diameters: $1.25cm$ (dotted lines), $2.5cm$ (solid lines), $5cm$ (dash-dot lines) and $30cm$ (dashed lines). From Mandhane *et al.* (1974).

7.2.3 Slurry flow regimes

As a further example, consider the flow regimes manifest by slurry (solid/liquid mixture) flow in a horizontal pipeline. When the particles are small so that their settling velocity is much less than the turbulent mixing velocities in the fluid and when the volume fraction of solids is low or moderate, the flow will be well-mixed. This is termed the *homogeneous* flow regime (figure 7.5) and typically only occurs in practical slurry pipelines when all the particle sizes are of the order of tens of microns or less. When somewhat larger particles are present, vertical gradients will occur in the concentration and the regime is termed *heterogeneous*; moreover the larger particles will tend to sediment faster and so a vertical size gradient will also occur. The limit of this heterogeneous flow regime occurs when the particles form a packed bed in the bottom of the pipe. When a packed bed develops, the flow regime is known as a *saltation* flow. In a saltation flow, solid material may be transported in two ways, either because the bed moves *en masse* or because material in suspension above the bed is carried along by the suspending fluid. Further analyses of these flow regimes, their transitions and their pressure gradients are included in sections 8.2.1, 8.2.2 and 8.2.3. For further detail, the reader is referred to Shook and Roco (1991), Zandi and Govatos (1967), and Zandi (1971).

7.2.4 Vertical pipe flow

When the pipe is oriented vertically, the regimes of gas/liquid flow are a little different as illustrated in figures 7.6 and 7.7 (see, for example, Hewitt and Hall Taylor 1970, Butterworth and Hewitt 1977, Hewitt 1982, Whalley 1987). Another vertical flow regime map is shown in figure 7.8, this one using momentum flux axes rather than volumetric or mass fluxes. Note the wide range of flow rates in Hewitt and Roberts (1969) flow regime map and the fact that they correlated both air/water data at atmospheric pressure and steam/water flow at high pressure.

Typical photographs of vertical gas/liquid flow regimes are shown in figure 7.9. At low gas volume fractions of the order of a few percent, the flow is an amalgam of individual ascending bubbles (left photograph). Note that the visual appearance is deceptive; most people would judge the volume fraction to be significantly larger than 1%. As the volume fraction is increased (the middle photograph has $\alpha = 4.5\%$), the flow becomes unstable at some critical volume fraction which in the case illustrated is about 15%. This instability produces large scale mixing motions that dominate the flow and have a scale comparable to the pipe diameter. At still larger volume fractions, large unsteady gas volumes accumulate within these mixing motions and produce the flow regime known as churn-turbulent flow (right photograph).

It should be added that flow regime information such as that presented in figure 7.8 appears to be valid both for flows that are not evolving with axial distance along the pipe and for flows, such as those in boiler tubes, in which the volume fraction is increasing with axial position. Figure 7.10 provides a sketch of the kind of evolution one might expect in a vertical boiler tube based on the flow regime maps given above. It is interesting to

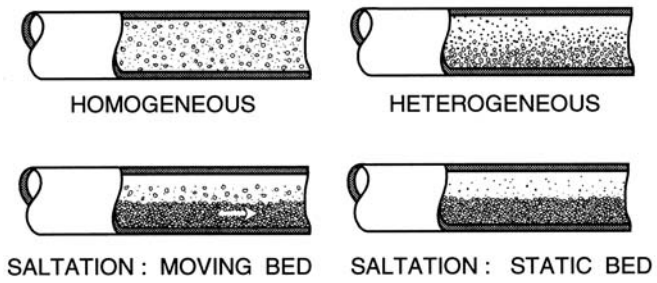

Figure 7.5. Flow regimes for slurry flow in a horizontal pipeline.

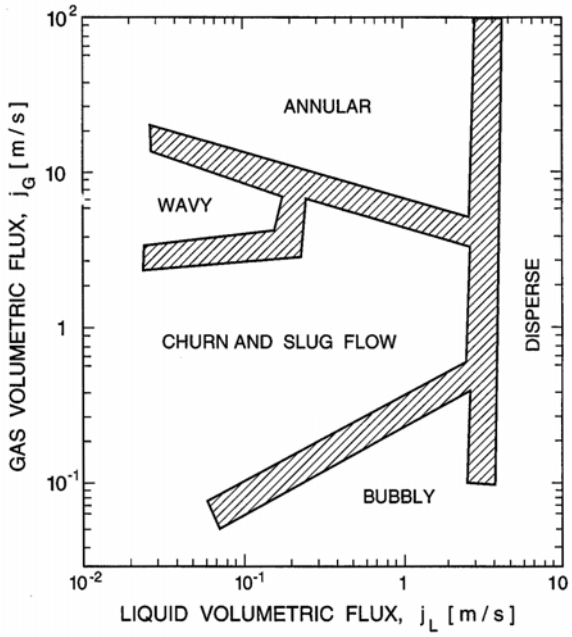

Figure 7.6. A flow regime map for the flow of an air/water mixture in a vertical, 2.5cm diameter pipe showing the experimentally observed transition regions hatched; the flow regimes are sketched in figure 7.7. Adapted from Weisman (1983).

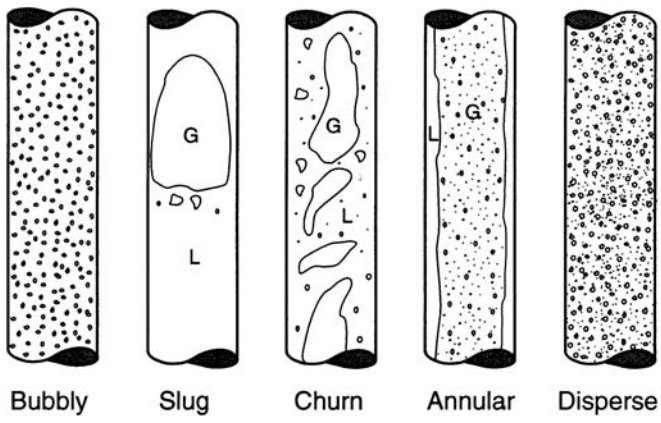

Figure 7.7. Sketches of flow regimes for two-phase flow in a vertical pipe. Adapted from Weisman (1983).

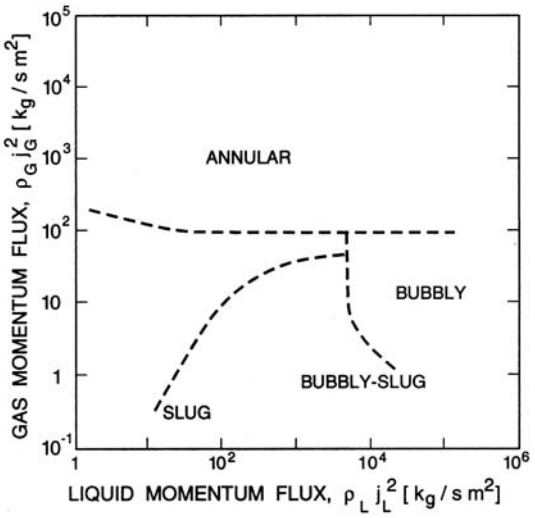

Figure 7.8. The vertical flow regime map of Hewitt and Roberts (1969) for flow in a $3.2cm$ diameter tube, validated for both air/water flow at atmospheric pressure and steam/water flow at high pressure.

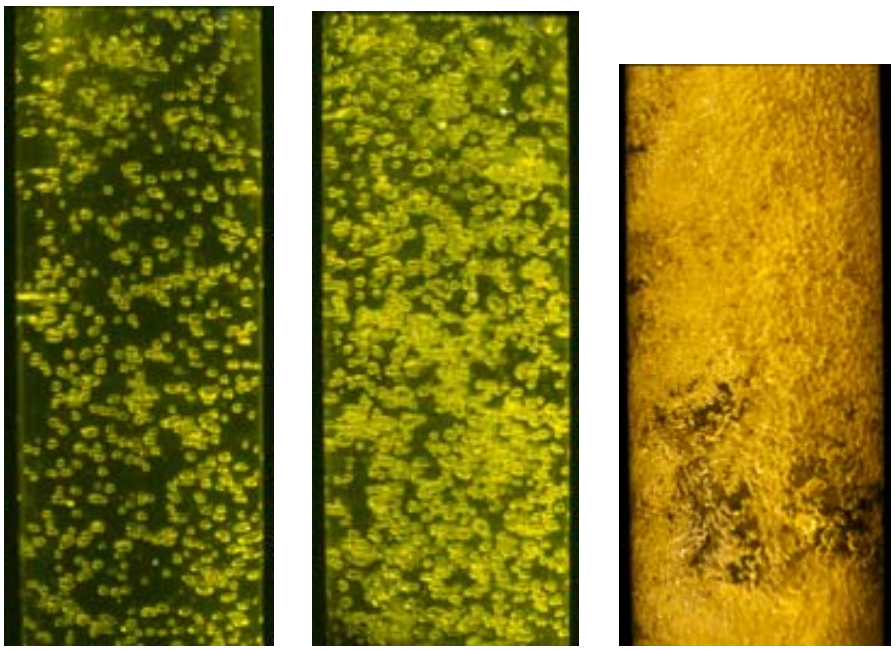

Figure 7.9. Photographs of air/water flow in a $10.2cm$ diameter vertical pipe (Kytömaa 1987). Left: 1% air; middle: 4.5% air; right: $> 15\%$ air.

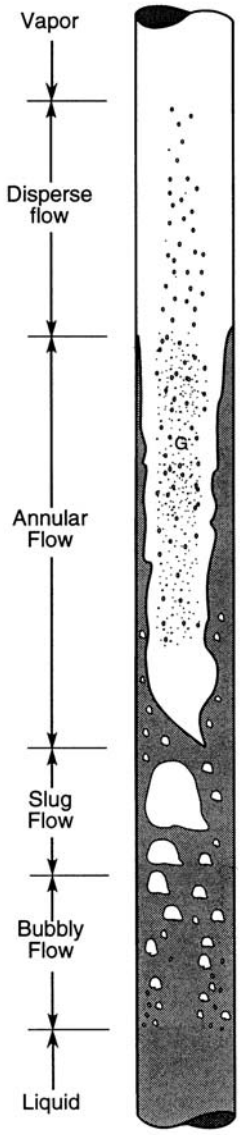

Figure 7.10. The evolution of the steam/water flow in a vertical boiler tube.

compare and contrast this flow pattern evolution with the inverted case of convective boiling surrounding a heated rod in figure 6.4.

7.2.5 Flow pattern classifications

One of the most fundamental characteristics of a multiphase flow pattern is the extent to which it involves global separation of the phases or components. At the two ends of the spectrum of separation characteristics are those flow patterns that are termed *disperse* and those that are termed *separated.* A *disperse* flow pattern is one in which one phase or component is widely distributed as drops, bubbles, or particles in the other *continuous* phase. On the other hand, a *separated* flow consists of separate, parallel streams of the two (or more) phases. Even within each of these limiting states there are various degrees of component separation. The asymptotic limit of a disperse flow in which the disperse phase is distributed as an infinite number of infinitesimally small particles, bubbles, or drops is termed a *homogeneous* multiphase flow. As discussed in sections 2.4.2 and 9.2 this limit implies zero relative motion between the phases. However, there are many practical disperse flows, such as bubbly or mist flow in a pipe, in which the flow is quite disperse in that the particle size is much smaller than the pipe dimensions but in which the relative motion between the phases is significant.

Within separated flows there are similar gradations or degrees of phase separation. The low velocity flow of gas and liquid in a pipe that consists of two single phase streams can be designated a *fully separated* flow. On the other hand, most annular flows in a vertical pipe consist of a film of liquid on the walls and a central core of gas that contains a significant number of liquid droplets. These droplets are an important feature of annular flow and therefore the flow can only be regarded as partially separated.

To summarize: one of the basic characteristics of a flow pattern is the degree of separation of the phases into streamtubes of different concentrations. The degree of separation will, in turn, be determined by (a) some balance between the fluid mechanical processes enhancing dispersion and those causing segregation, or (b) the initial conditions or mechanism of generation of the multiphase flow, or (c) some mix of both effects. In the section 7.3.1 we shall discuss the fluid mechanical processes referred to in (a).

A second basic characteristic that is useful in classifying flow patterns is the level of intermittency in the volume fraction. Examples of intermittent flow patterns are slug flows in both vertical and horizontal pipe flows and the occurrence of interfacial waves in horizontal separated flow. The first separation characteristic was the degree of separation of the phases between streamtubes; this second, intermittency characteristic, can be viewed as the degree of periodic separation in the streamwise direction. The slugs or waves are kinematic or concentration waves (sometimes called continuity waves)

and a general discussion of the structure and characteristics of such waves is contained in chapter 16. Intermittency is the result of an instability in which kinematic waves grow in an otherwise nominally steady flow to create significant streamwise separation of the phases.

In the rest of this chapter we describe how these ideas of cross-streamline separation and intermittency can lead to an understanding of the limits of specific multiphase flow regimes. The mechanics of limits on disperse flow regimes are discussed first in sections 7.3 and 7.4. Limits on separated flow regimes are outlined in section 7.5.

7.3 LIMITS OF DISPERSE FLOW REGIMES

7.3.1 Disperse phase separation and dispersion

In order to determine the limits of a disperse phase flow regime, it is necessary to identify the dominant processes enhancing separation and those causing dispersion. By far the most common process causing phase separation is due to the difference in the densities of the phases and the mechanisms are therefore functions of the ratio of the density of the disperse phase to that of the continuous phase, ρ_D/ρ_C. Then the buoyancy forces caused either by gravity or, in a non-uniform or turbulent flow by the Lagrangian fluid accelerations will create a relative velocity between the phases whose magnitude will be denoted by W_p. Using the analysis of section 2.4.2, we can conclude that the ratio W_p/U (where U is a typical velocity of the mean flow) is a function only of the Reynolds number, $Re = 2UR/\nu_C$, and the parameters X and Y defined by equations 2.91 and 2.92. The particle size, R, and the streamwise extent of the flow, ℓ, both occur in the dimensionless parameters Re, X, and Y. For low velocity flows in which $U^2/\ell \ll g$, ℓ is replaced by g/U^2 and hence a Froude number, gR/U^2, rather than R/ℓ appears in the parameter X. This then establishes a velocity, W_p, that characterizes the relative motion and therefore the phase separation due to density differences.

As an aside we note that there are some fluid mechanical phenomena that can cause phase separation even in the absence of a density difference. For example, Ho and Leal (1974) explored the migration of neutrally buoyant particles in shear flows at low Reynolds numbers. These effects are usually sufficiently weak compared with those due to density differences that they can be neglected in many applications.

In a quiescent multiphase mixture the primary mechanism of phase separation is sedimentation (see chapter 16) though more localized separation

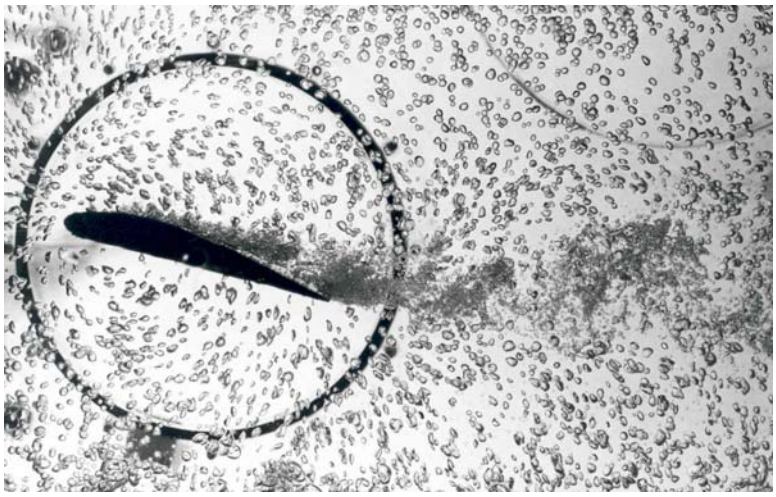

Figure 7.11. Bubbly flow around a NACA 4412 hydrofoil (10cm chord) at an angle of attack; flow is from left to right. From the work of Ohashi *et al.*, reproduced with the author's permission.

can also occur as a result of the inhomogeneity instability described in section 7.4. In flowing mixtures the mechanisms are more complex and, in most applications, are controlled by a balance between the buoyancy/gravity forces and the hydrodynamic forces. In high Reynolds number, turbulent flows, the turbulence can cause either dispersion or segregation. Segregation can occur when the relaxation time for the particle or bubble is comparable with the typical time of the turbulent fluid motions. When $\rho_D/\rho_C \gg 1$ as for example with solid particles suspended in a gas, the particles are centrifuged out of the more intense turbulent eddies and collect in the shear zones in between (see for example, Squires and Eaton 1990, Elghobashi and Truesdell 1993). On the other hand when $\rho_D/\rho_C \ll 1$ as for example with bubbles in a liquid, the bubbles tend to collect in regions of low pressure such as in the wake of a body or in the centers of vortices (see for example Pan and Banerjee 1997). We previously included a photograph (figure 1.6) showing heavier particles centrifuged out of vortices in a turbulent channel flow. Here, as a counterpoint, we include the photograph, figure 7.11, from Ohashi *et al.* (1990) showing the flow of a bubbly mixture around a hydrofoil. Note the region of higher void fraction (more than four times the upstream void fraction according to the measurements) in the wake on the suction side of the foil. This accumulation of bubbles on the suction side of a foil or pump blade has importance consequences for performance as discussed in section 7.3.3.

Counteracting the above separation processes are dispersion processes. In many engineering contexts the principal dispersion is caused by the turbulent or other unsteady motions in the continuous phase. Figure 7.11 also illustrates this process for the concentrated regions of high void fraction in the wake are dispersed as they are carried downstream. The shear created by unsteady velocities can also cause either fission or fusion of the disperse phase bubbles, drops, or particles, but we shall delay discussion of this additional complexity until the next section. For the present it is only necessary to characterize the mixing motions in the continuous phase by a typical velocity, W_t. Then the degree of separation of the phases will clearly be influenced by the relative magnitudes of W_p and W_t, or specifically by the ratio W_p/W_t. Disperse flow will occur when $W_p/W_t \ll 1$ and separated flow when $W_p/W_t \gg 1$. The corresponding flow pattern boundary should be given by some value of W_p/W_t of order unity. For example, in slurry flows in a horizontal pipeline, Thomas (1962) suggested a value of W_p/W_t of 0.2 based on his data.

7.3.2 Example: horizontal pipe flow

As a quantitative example, we shall pursue the case of the flow of a two-component mixture in a long horizontal pipe. The separation velocity, W_p, due to gravity, g, would then be given qualitatively by equation 2.74 or 2.83, namely

$$W_p = \frac{2R^2 g}{9\nu_C}\left(\frac{\Delta\rho}{\rho_C}\right) \quad \text{if} \quad 2W_pR/\nu_C \ll 1 \tag{7.1}$$

or

$$W_p = \left\{\frac{2}{3}\frac{Rg}{C_D}\frac{\Delta\rho}{\rho_C}\right\}^{\frac{1}{2}} \quad \text{if} \quad 2W_pR/\nu_C \gg 1 \tag{7.2}$$

where R is the particle, droplet, or bubble radius, ν_C, ρ_C are the kinematic viscosity and density of the continuous fluid, and $\Delta\rho$ is the density difference between the components. Furthermore, the typical turbulent velocity will be some function of the friction velocity, $(\tau_w/\rho_C)^{\frac{1}{2}}$, and the volume fraction, α, of the disperse phase. The effect of α is less readily quantified so, for the present, we concentrate on dilute systems ($\alpha \ll 1$) in which

$$W_t \approx \left(\frac{\tau_w}{\rho_C}\right)^{\frac{1}{2}} = \left\{\frac{d}{4\rho_C}\left(-\frac{dp}{ds}\right)\right\}^{\frac{1}{2}} \tag{7.3}$$

where d is the pipe diameter and dp/ds is the pressure gradient. Then the transition condition, $W_p/W_t = K$ (where K is some number of order unity) can be rewritten as

$$\left(-\frac{dp}{ds}\right) \approx \frac{4\rho_C}{K^2 d} W_p^2 \tag{7.4}$$

$$\approx \frac{16}{81K^2} \frac{\rho_C R^4 g^2}{\nu_C^2 d} \left(\frac{\Delta\rho}{\rho_C}\right)^2 \quad \text{for} \quad 2W_p R/\nu_C \ll 1 \tag{7.5}$$

$$\approx \frac{32}{3K^2} \frac{\rho_C R g}{C_D d} \left(\frac{\Delta\rho}{\rho_C}\right) \quad \text{for} \quad 2W_p R/\nu_C \gg 1 \tag{7.6}$$

In summary, the expression on the right hand side of equation 7.5 (or 7.6) yields the pressure drop at which W_p/W_t exceeds the critical value of K and the particles will be maintained in suspension by the turbulence. At lower values of the pressure drop the particles will settle out and the flow will become separated and stratified.

This criterion on the pressure gradient may be converted to a criterion on the flow rate by using some version of the turbulent pipe flow relation between the pressure gradient and the volume flow rate, j. For example, one could conceive of using, as a first approximation, a typical value of the turbulent friction factor, $f = \tau_w/\frac{1}{2}\rho_C j^2$ (where j is the total volumetric flux). In the case of $2W_p R/\nu_C \gg 1$, this leads to a critical volume flow rate, $j = j_c$, given by

$$j_c = \left\{ \frac{8}{3K^2 f} \frac{gD}{C_D} \frac{\Delta\rho}{\rho_C} \right\}^{\frac{1}{2}} \tag{7.7}$$

With $8/3K^2 f$ replaced by an empirical constant, this is the general form of the critical flow rate suggested by Newitt *et al.* (1955) for horizontal slurry pipeline flow; for $j > j_c$ the flow regime changes from saltation flow to heterogeneous flow (see figure 7.5). Alternatively, one could write this nondimensionally using a Froude number defined as $Fr = j_c/(gd)^{\frac{1}{2}}$. Then the criterion yields a critical Froude number given by

$$Fr^2 = \frac{8}{3K^2 f C_D} \frac{\Delta\rho}{\rho_C} \tag{7.8}$$

If the common expression for the turbulent friction factor, namely $f =$

$0.31/(jd/\nu_C)^{\frac{1}{4}}$ is used in equation 7.7, that expression becomes

$$j_c = \left\{ \frac{17.2}{K^2 C_D} \frac{gRd^{\frac{1}{4}}}{\nu_C^{\frac{1}{4}}} \frac{\Delta\rho}{\rho_C} \right\}^{\frac{4}{7}} \tag{7.9}$$

A numerical example will help relate this criterion 7.9 to the boundary of the disperse phase regime in the flow regime maps. For the case of figure 7.3 and using for simplicity, $K = 1$ and $C_D = 1$, then with a drop or bubble size, $R = 3mm$, equation 7.9 gives a value of j_c of $3m/s$ when the continuous phase is liquid (bubbly flow) and a value of $40m/s$ when the continuous phase is air (mist flow). These values are in good agreement with the total volumetric flux at the boundary of the disperse flow regime in figure 7.3 which, at low j_G, is about $3m/s$ and at higher j_G (volumetric qualities above 0.5) is about $30 - 40m/s$.

Another approach to the issue of the critical velocity in slurry pipeline flow is to consider the velocity required to fluidize a packed bed in the bottom of the pipe (see, for example, Durand and Condolios (1952) or Zandi and Govatos (1967)). This is described further in section 8.2.3.

7.3.3 Particle size and particle fission

In the preceding sections, the transition criteria determining the limits of the disperse flow regime included the particle, bubble or drop size or, more specifically, the dimensionless parameter $2R/d$ as illustrated by the criteria of equations 7.5, 7.6 and 7.9. However, these criteria require knowledge of the size of the particles, $2R$, and this is not always accessible particularly in bubbly flow. Even when there may be some knowledge of the particle or bubble size in one region or at one time, the various processes of fission and fusion need to be considered in determining the appropriate $2R$ for use in these criteria. One of the serious complications is that the size of the particles, bubbles or drops is often determined by the flow itself since the flow shear tends to cause fission and therefore limit the maximum size of the surviving particles. Then the flow regime may depend upon the particle size that in turn depends on the flow and this two-way interaction can be difficult to unravel. Figure 7.11 illustrates this problem since one can observe many smaller bubbles in the flow near the suction surface and in the wake that clearly result from fission in the highly sheared flow near the suction surface. Another example from the flow in pumps is described in the next section.

When the particles are very small, a variety of forces may play a role in determining the effective particle size and some comments on these are included later in section 7.3.7. But often the bubbles or drops are sufficiently large that the dominant force resisting fission is due to surface tension while the dominant force promoting fission is the shear in the flow. We will confine the present discussion to these circumstances. Typical regions of high shear occur in boundary layers, in vortices or in turbulence. Frequently, the larger drops or bubbles are fissioned when they encounter regions of high shear and do not subsequently coalesce to any significant degree. Then, the characteristic force resisting fission would be given by SR while the typical shear force causing fission might be estimated in several ways. For example, in the case of pipe flow the typical shear force could be characterized by $\tau_w R^2$. Then, assuming that the flow is initiated with larger particles that are then fissioned by the flow, we would estimate that $R = S/\tau_w$. This will be used in the next section to estimate the limits of the bubbly or mist flow regime in pipe flows.

In other circumstances, the shearing force in the flow might be described by $\rho_C(\dot{\gamma}R)^2R^2$ where $\dot{\gamma}$ is the typical shear rate and ρ_C is the density of the continuous phase. This expression for the fission force assumes a high Reynolds number in the flow around the particle or explicitly that $\rho_C\dot{\gamma}R^2/\mu_C \gg 1$ where μ_C is the dynamic viscosity of the continuous phase. If, on the other hand, $\rho_C\dot{\gamma}R^2/\mu_C \ll 1$ then a more appropriate estimate of the fission force would be $\mu_C\dot{\gamma}R^2$. Consequently, the maximum particle size, R_m, one would expect to see in the flow in these two regimes would be

$$R_m = \left\{\frac{S}{\mu_C\dot{\gamma}}\right\} \quad \text{for} \quad \rho_C\dot{\gamma}R^2/\mu_C \ll 1$$

$$\underline{\text{or}} \quad \left\{\frac{S}{\rho_C\dot{\gamma}^2}\right\}^{\frac{1}{3}} \quad \text{for} \quad \rho_C\dot{\gamma}R^2/\mu_C \gg 1 \tag{7.10}$$

respectively. Note that in both instances the maximum size decreases with increasing shear rate.

7.3.4 Examples of flow-determined bubble size

An example of the use of the above relations can be found in the important area of two-phase pump flows and we quote here data from studies of the pumping of bubbly liquids. The issue here is the determination of the volume fraction at which the pump performance is seriously degraded by the presence of the bubbles. It transpires that, in most practical pumping

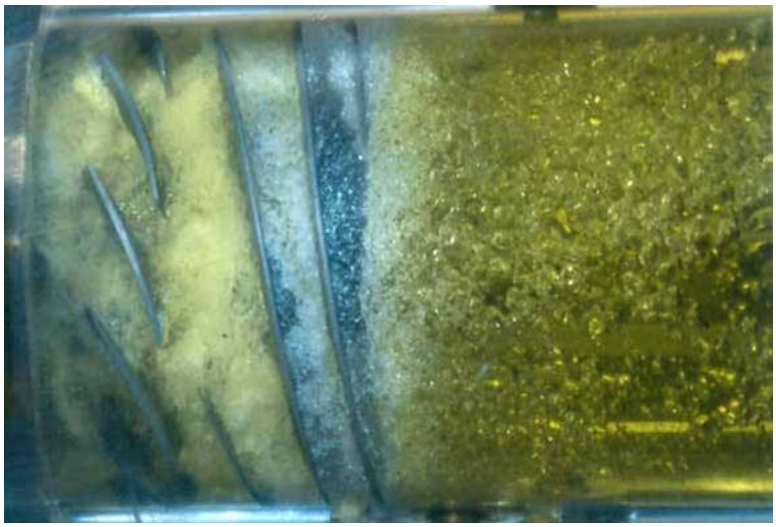

Figure 7.12. A bubbly air/water mixture (volume fraction about 4%) entering an axial flow impeller (a 10.2cm diameter scale model of the SSME low pressure liquid oxygen impeller) from the right. The inlet plane is roughly in the center of the photograph and the tips of the blades can be seen to the left of the inlet plane.

situations, the turbulence and shear at inlet and around the leading edges of the blades of the pump (or other turbomachine) tend to fission the bubbles and thus determine the size of the bubbles in the blade passages. An illustration is included in figure 7.12 which shows an air/water mixture progressing through an axial flow impeller; the bubble size downstream of the inlet plane is much smaller that that approaching the impeller.

The size of the bubbles within the blade passages is important because it is the migration and coalescence of these bubbles that appear to cause degradation in the performance. Since the velocity of the relative motion depends on the bubble size, it follows that the larger the bubbles the more likely it is that large voids will form within the blade passage due to migration of the bubbles toward regions of lower pressure (Furuya 1985, Furuya and Maekawa 1985). As Patel and Runstadler (1978) observed during experiments on centrifugal pumps and rotating passages, regions of low pressure occur not only on the suction sides of the blades but also under the shroud of a centrifugal pump. These large voids or gas-filled wakes can cause substantial changes in the deviation angle of the flow leaving the impeller and hence lead to substantial degradation in the pump performance.

The key is therefore the size of the bubbles in the blade passages and some valuable data on this has been compiled by Murakami and Minemura (1977,

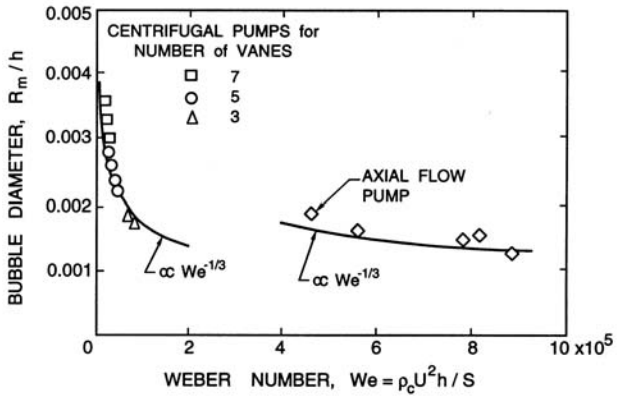

Figure 7.13. The bubble sizes, R_m, observed in the blade passages of centrifugal and axial flow pumps as a function of Weber number where h is the blade spacing (adapted from Murakami and Minemura 1978).

1978) for both axial and centrifugal pumps. This is summarized in figure 7.4 where the ratio of the observed bubble size, R_m, to the blade spacing, h, is plotted against the Weber number, $We = \rho_C U^2 h/S$ (U is the blade tip velocity). Rearranging the first version of equation 7.10, estimating that the inlet shear is proportional to U/h and adding a proportionality constant, C, since the analysis is qualitative, we would expect that $R_m = C/We^{\frac{1}{3}}$. The dashed lines in figure 7.13 are examples of this prediction and exhibit behavior very similar to the experimental data. In the case of the axial pumps, the effective value of the coefficient, $C = 0.15$.

A different example is provided by cavitating flows in which the highest shear rates occur during the collapse of the cavitation bubbles. As discussed in section 5.2.3, these high shear rates cause individual cavitation bubbles to fission into many smaller fragments so that the bubble size emerging from the region of cavitation bubble collapse is much smaller than the size of the bubbles entering that region. The phenomenon is exemplified by figure 7.14 which shows the growth of the cavitating bubbles on the suction surface of the foil, the collapse region near the trailing edge and the much smaller bubbles emerging from the collapse region. Some analysis of the fission due to cavitation bubble collapse is contained in Brennen (2002).

7.3.5 Bubbly or mist flow limits

Returning now to the issue of determining the boundaries of the bubbly (or mist flow) regime in pipe flows, and using the expression $R = S/\tau_w$ for the

Figure 7.14. Traveling bubble cavitation on the surface of a NACA 4412 hydrofoil at zero incidence angle, a speed of 13.7 m/s and a cavitation number of 0.3. The flow is from left to right, the leading edge of the foil is just to the left of the white glare patch on the surface, and the chord is 7.6cm (Kermeen 1956).

bubble size in equation 7.6, the transition between bubbly disperse flow and separated (or partially separated flow) will be described by the relation

$$\left\{\frac{-\frac{dp}{ds}}{g\Delta\rho}\right\}^{\frac{1}{2}}\left\{\frac{S}{gd^2\Delta\rho}\right\}^{-\frac{1}{4}} = \left\{\frac{64}{3K^2C_D}\right\}^{\frac{1}{4}} = \text{constant} \qquad (7.11)$$

This is the analytical form of the flow regime boundary suggested by Taitel and Dukler (1976) for the transition from disperse bubbly flow to a more separated state. Taitel and Dukler also demonstrate that when the constant in equation 7.11 is of order unity, the boundary agrees well with that observed experimentally by Mandhane *et al.* (1974). This agreement is shown in figure 7.3. The same figure serves to remind us that there are other transitions that Taitel and Dukler were also able to model with qualitative arguments. They also demonstrate, as mentioned earlier, that each of these transitions typically scale differently with the various non-dimensional parameters governing the characteristics of the flow and the fluids.

7.3.6 Other bubbly flow limits

As the volume fraction of gas or vapor is increased, a bubbly flow usually transitions to a mist flow, a metamorphosis that involves a switch in the con-

tinuous and disperse phases. However, there are several additional comments on this metamorphosis that need to be noted.

First, at very low flow rates, there are circumstances in which this transition does not occur at all and the bubbly flow becomes a foam. Though the precise conditions necessary for this development are not clear, foams and their rheology have been the subject of considerable study. The mechanics of foams are beyond the scope of this book; the reader is referred to the review by Kraynik (1988) and the book by Weaire and Hutzler (2001).

Second, though it is rarely mentioned, the reverse transition from mist flow to bubbly flow as the volume fraction decreases involves energy dissipation and an increase in pressure. This transition has been called a *mixing shock* (Witte 1969) and typically occurs when a droplet flow with significant relative motion transitions to a bubbly flow with negligible relative motion. Witte (1969) has analyzed these mixing shocks and obtains expressions for the compression ratio across the mixing shock as a function of the upstream slip and Euler number.

7.3.7 Other particle size effects

In sections 7.3.3 and 7.3.5 we outlined one class of circumstances in which bubble fission is an important facet of the disperse phase dynamics. It is, however, important, to add, even if briefly, that there are many other mechanisms for particle fission and fusion that may be important in a disperse phase flow. When the particles are sub-micron or micron sized, intermolecular and electromagnetic forces can become critically important in determining particle aggregation in the flow. These phenomena are beyond the scope of this book and the reader is referred to texts such as Friedlander (1977) or Flagan and Seinfeld (1988) for information on the effects these forces have on flows involving particles and drops. It is however valuable to add that gas-solid suspension flows with larger particles can also exhibit important effects as a result of electrical charge separation and the forces that those charges create between particles or between the particles and the walls of the flow. The process of electrification or charge separation is often a very important feature of such flows (Boothroyd 1971). Pneumatically driven flows in grain elevators or other devices can generate huge electropotential differences (as large as hundreds of kilovolts) that can, in turn, cause spark discharges and consequently dust explosions. In other devices, particularly electrophotographic copiers, the charge separation generated in a flowing toner/carrier mixture is a key feature of such devices. Electromagnetic and intermolecu-

lar forces can also play a role in determining the bubble or droplet size in gas-liquid flows (or flows of immiscible liquid mixtures).

7.4 INHOMOGENEITY INSTABILITY

In section 7.3.1 we presented a qualitative evaluation of phase separation processes driven by the combination of a density difference and a fluid acceleration. Such a combination does not necessarily imply separation within a homogeneous quiescent mixture (except through sedimentation). However, it transpires that local phase separation may also occur through the development of an inhomogeneity instability whose origin and consequences we describe in the next two sections.

7.4.1 Stability of disperse mixtures

It transpires that a homogeneous, quiescent multiphase mixture may be internally unstable as a result of gravitationally-induced relative motion. This instability was first described for fluidized beds by Jackson (1963). It results in horizontally-oriented, vertically-propagating volume fraction waves or layers of the disperse phase. To evaluate the stability of a uniformly dispersed two component mixture with uniform relative velocity induced by gravity and a density difference, Jackson constructed a model consisting of the following system of equations:

1. The number continuity equation 1.30 for the particles (density, ρ_D, and volume fraction, $\alpha_D = \alpha$):

$$\frac{\partial \alpha}{\partial t} + \frac{\partial (\alpha u_D)}{\partial y} = 0 \tag{7.12}$$

   where all velocities are in the vertically upward direction.
2. Volume continuity for the suspending fluid (assuming constant density, ρ_C, and zero mass interaction, $\mathcal{I}_N = 0$)

$$\frac{\partial \alpha}{\partial t} - \frac{\partial ((1-\alpha) u_C)}{\partial y} = 0 \tag{7.13}$$

3. Individual phase momentum equations 1.42 for both the particles and the fluid assuming constant densities and no deviatoric stress:

$$\rho_D \alpha \left\{ \frac{\partial u_D}{\partial t} + u_D \frac{\partial u_D}{\partial y} \right\} = -\alpha \rho_D g + \mathcal{F}_D \tag{7.14}$$

$$\rho_C(1-\alpha)\left\{\frac{\partial u_C}{\partial t}+u_C\frac{\partial u_C}{\partial y}\right\}=-(1-\alpha)\rho_C g-\frac{\partial p}{\partial y}-\mathcal{F}_D \tag{7.15}$$

4. A force interaction term of the form given by equation 1.44. Jackson constructs a component, $\mathcal{F}'_{Dk}$, due to the relative motion of the form

$$\mathcal{F}'_D=q(\alpha)(1-\alpha)(u_C-u_D) \tag{7.16}$$

where q is assumed to be some function of α. Note that this is consistent with a low Reynolds number flow.

Jackson then considered solutions of these equations that involve small, linear perturbations or waves in an otherwise homogeneous mixture. Thus the flow was decomposed into:

1. A uniform, homogeneous fluidized bed in which the mean values of u_D and u_C are respectively zero and some adjustable constant. To maintain generality, we will characterize the relative motion by the drift flux, $j_{CD}=\alpha(1-\alpha)u_C$.
2. An unsteady linear perturbation in the velocities, pressure and volume fraction of the form $exp\{i\kappa y+(\zeta-i\omega)t\}$ that models waves of wavenumber, κ, and frequency, ω, traveling in the y direction with velocity ω/κ and increasing in amplitude at a rate given by ζ.

Substituting this decomposition into the system of equations described above yields the following expression for $(\zeta-i\omega)$:

$$(\zeta-i\omega)\frac{j_{CD}}{g}=\pm K_2\{1+4iK_3+4K_1K_3^2-4iK_3(1+K_1)K_4\}^{\frac{1}{2}}-K_2(1+2iK_3) \tag{7.17}$$

where the constants K_1 through K_3 are given by

$$K_1=\frac{\rho_D}{\rho_C}\frac{(1-\alpha)}{\alpha} \quad ; \quad K_2=\frac{(\rho_D-\rho_C)\alpha(1-\alpha)}{2\{\rho_D(1-\alpha)+\rho_C\alpha\}}$$

$$K_3=\frac{\kappa\, j_{CD}^2}{g\alpha(1-\alpha)^2\{\rho_D/\rho_C-1\}} \tag{7.18}$$

and K_4 is given by

$$K_4=2\alpha-1+\frac{\alpha(1-\alpha)}{q}\frac{dq}{d\alpha} \tag{7.19}$$

It transpires that K_4 is a critical parameter in determining the stability and it, in turn, depends on how q, the factor of proportionality in equation 7.16, varies with α. Here we examine two possible functions, $q(\alpha)$. The Carman-Kozeny equation 2.96 for the pressure drop through a packed bed is

appropriate for slow viscous flow and leads to $q \propto \alpha^2/(1-\alpha)^2$; from equation 7.19 this yields $K_4 = 2\alpha + 1$ and is an example of low Reynolds number flow. As a representative example of higher Reynolds number flow we take the relation 2.100 due to Wallis (1969) and this leads to $q \propto \alpha/(1-\alpha)^{b-1}$ (recall Wallis suggests $b = 3$); this yields $K_4 = b\alpha$. We will examine both of these examples of the form of $q(\alpha)$.

Note that the solution 7.17 yields the non-dimensional frequency and growth rate of waves with wavenumber, κ, as functions of just three dimensionless variables, the volume fraction, α, the density ratio, ρ_D/ρ_C, and the relative motion parameter, $j_{CD}/(g/\kappa)^{\frac{1}{2}}$, similar to a Froude number. Note also that equation 7.17 yields two roots for the dimensionless frequency, $\omega j_{CD}/g$, and growth rate, $\zeta j_{CD}/g$. Jackson demonstrates that the negative sign choice is an attenuated wave; consequently we focus exclusively on the positive sign choice that represents a wave that propagates in the direction of the drift flux, j_{CD}, and grows exponentially with time. It is also easy to see that the growth rate tends to infinity as $\kappa \to \infty$. However, it is meaningless to consider wavelengths less than the inter-particle distance and therefore the focus should be on waves of this order since they will predominate. Therefore, in the discussion below, it is assumed that the κ^{-1} values of primary interest are of the order of the typical inter-particle distance.

Figure 7.15 presents typical dimensionless growth rates for various values of the parameters α, ρ_D/ρ_C, and $j_{CD}/(g/\kappa)^{\frac{1}{2}}$ for both the Carman-Kozeny and Wallis expressions for K_4. In all cases the growth rate increases with the wavenumber κ, confirming the fact that the fastest growing wavelength is the smallest that is relevant. We note, however, that a more complete linear analysis by Anderson and Jackson (1968) (see also Homsy *et al.* 1980, Jackson 1985, Kytömaa 1987) that includes viscous effects yields a wavelength that has a maximum growth rate. Figure 7.15 also demonstrates that the effect of void fraction is modest; though the lines for $\alpha = 0.5$ lie below those for $\alpha = 0.1$ this must be weighed in conjunction with the fact that the inter-particle distance is greater in the latter case. Gas and liquid fluidized beds are typified by ρ_D/ρ_C values of 3000 and 3 respectively; since the lines for these two cases are not far apart, the primary difference is the much larger values of j_{CD} in gas-fluidized beds. Everything else being equal, increasing j_{CD} means following a line of slope 1 in figure 7.15 and this implies much larger values of the growth rate in gas-fluidized beds. This is in accord with the experimental observations.

As a postscript, it must be noted that the above analysis leaves out many effects that may be consequential. As previously mentioned, the inclusion

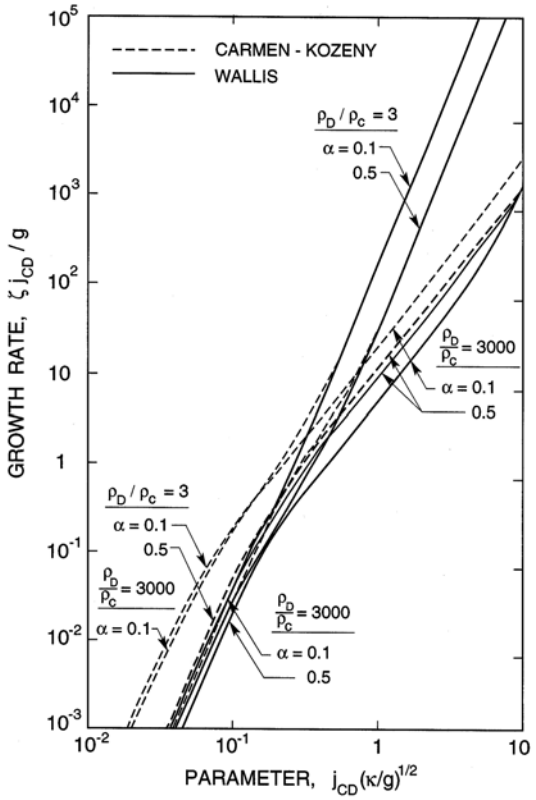

Figure 7.15. The dimensionless growth rate $\zeta j_{CD}/g$ plotted against the parameter $j_{CD}/(g/\kappa)^{\frac{1}{2}}$ for various values of α and ρ_D/ρ_C and for both $K_4 = 2\alpha + 1$ and $K_4 = 3\alpha$.

of viscous effects is important at least for lower Reynolds number flows. At higher particle Reynolds numbers, even more complex interactions can occur as particles encounter the wakes of other particles. For example, Fortes *et al.* (1987) demonstrated the complexity of particle-particle interactions under those circumstances and Joseph (1993) provides a summary of how the inhomogeneities or volume fraction waves evolve with such interactions. General analyses of kinematic waves are contained in chapter 16 and the reader is referred to that chapter for details.

7.4.2 Inhomogeneity instability in vertical flows

In vertical flows, the inhomogeneity instability described in the last section will mean the development of intermittency in the volume fraction. The short

term result of this instability is the appearance of vertically propagating, horizontally oriented kinematic waves (see chapter 16) in otherwise nominally steady flows. They have been most extensively researched in fluidized beds but have also be observed experimentally in vertical bubbly flows by Bernier (1982), Boure and Mercadier (1982), Kytomaa and Brennen (1990) (who also examined solid/liquid mixtures at large Reynolds numbers) and analyzed by Biesheuvel and Gorissen (1990). (Some further comment on these bubbly flow measurements is contained in section 16.2.3.)

As they grow in amplitude these wave-like volume fraction perturbations seem to evolve in several ways depending on the type of flow and the manner in which it is initiated. In turbulent gas/liquid flows they result in large gas volumes or slugs with a size close to the diameter of the pipe. In some solid/liquid flows they produce a series of periodic vortices, again with a dimension comparable with that of the pipe diameter. But the long term consequences of the inhomogeneity instability have been most carefully studied in the context of fluidized beds. Following the work of Jackson (1963), El-Kaissy and Homsy (1976) studied the evolution of the kinematic waves experimentally and observed how they eventually lead, in fluidized beds, to three-dimensional structures known as *bubbles* . These are *not* gas bubbles but three-dimensional, bubble-like zones of low particle concentration that propagate upward through the bed while their structure changes relatively slowly. They are particularly evident in wide fluidized beds where the lateral dimension is much larger than the typical interparticle distance. Sometimes bubbles are directly produced by the sparger or injector that creates the multiphase flow. This tends to be the case in gas-fluidized beds where, as illustrated in the preceding section, the rate of growth of the inhomogeneity is much greater than in liquid fluidized beds and thus bubbles are instantly formed.

Because of their ubiquity in industrial processes, the details of the three-dimensional flows associated with fluidized-bed bubbles have been extensively studied both experimentally (see, for example, Davidson and Harrison 1963, Davidson *et al.* 1985) and analytically (Jackson 1963, Homsy *et al.* 1980). Roughly spherical or spherical cap in shape, these zones of low solids volume fraction always rise in a fluidized bed (see figure 7.16). When the density of bubbles is low, single bubbles are observed to rise with a velocity, W_B, given empirically by Davidson and Harrison (1963) as

$$W_B = 0.71 g^{\frac{1}{2}} V_B^{\frac{1}{6}} \tag{7.20}$$

where V_B is the volume of the bubble. Both the shape and rise velocity

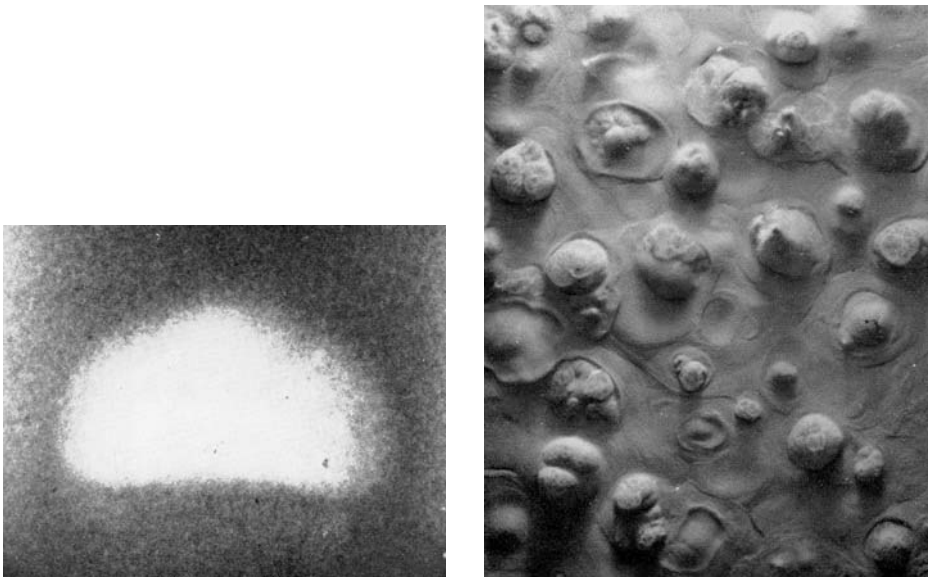

Figure 7.16. Left: X-ray image of fluidized bed bubble (about $5cm$ in diameter) in a bed of glass beads (courtesy of P.T.Rowe). Right: View from above of bubbles breaking the surface of a sand/air fluidized bed (courtesy of J.F.Davidson).

have many similarities to the spherical cap bubbles discussed in section 3.2.2. The rise velocity, W_B may be either faster or slower than the upward velocity of the suspending fluid, u_C, and this implies two types of bubbles that Catipovic *et al.* (1978) call *fast* and *slow* bubbles respectively. Figure 7.17 qualitatively depicts the nature of the streamlines of the flow relative to the bubbles for fast and slow bubbles. The same paper provides a flow regime map, figure 7.18 indicating the domains of fast bubbles, slow bubbles and rapidly growing bubbles. When the particles are smaller other forces become important, particularly those that cause particles to stick together. In gas fluidized beds the flow regime map of Geldart (1973), reproduced as figure 7.19, is widely used to determine the flow regime. With very small particles (Group C) the cohesive effects dominate and the bed behaves like a plug, though the suspending fluid may create holes in the plug. With somewhat larger particles (Group A), the bed exhibits considerable expansion before bubbling begins. Group B particles exhibit bubbles as soon as fluidization begins (fast bubbles) and, with even larger particles (Group D), the bubbles become slow bubbles.

Aspects of the flow regime maps in figures 7.18 and 7.19 qualitatively reflect the results of the instability analysis of the last section. Larger particles

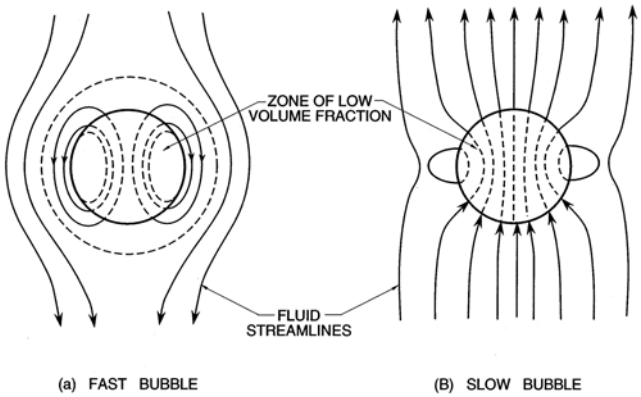

Figure 7.17. Sketches of the fluid streamlines relative to a fluidized bed *bubble* of low volume fraction for a *fast* bubble (left) and a *slow* bubble. Adapted from Catipovic *et al.* (1978).

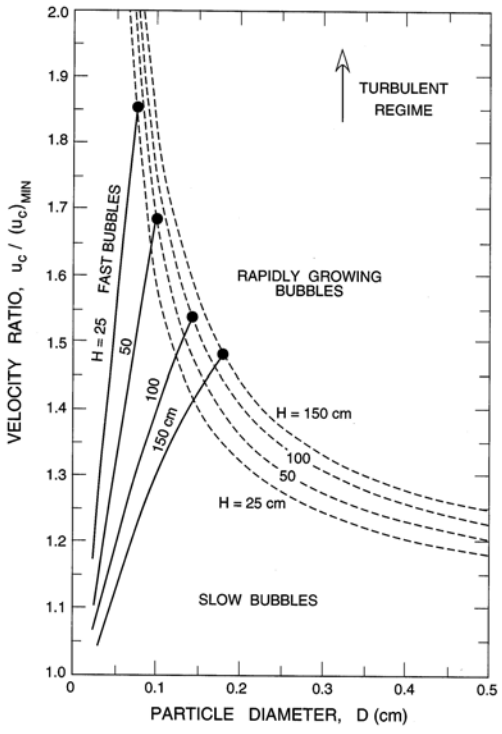

Figure 7.18. Flow regime map for fluidized beds with large particles (diameter, D) where $(u_C)_{min}$ is the minimum fluidization velocity and H is the height of the bed. Adapted from Catipovic *et al.* (1978).

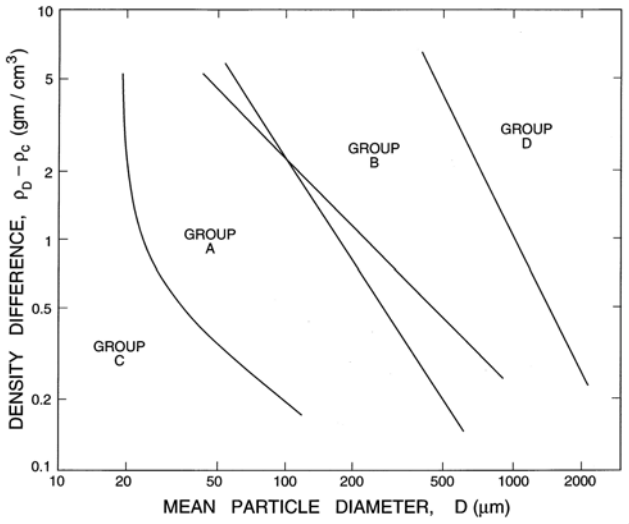

Figure 7.19. Flow regime map for fluidized beds with small particles (diameter, D). Adapted from Geldart (1973).

and larger fluid velocities imply larger j_{CD} values and therefore, according to instability analysis, larger growth rates. Thus, in the upper right side of both figures we find rapidly growing bubbles. Moreover, in the instability analysis it transpires that the ratio of the wave speed, ω/κ (analogous to the bubble velocity) to the typical fluid velocity, j_{CD}, is a continuously decreasing function of the parameter, $j_{CD}/(g/\kappa)^{\frac{1}{2}}$. Indeed, $\omega/j_{CD}\kappa$ decreases from values greater than unity to values less than unity as $j_{CD}/(g/\kappa)^{\frac{1}{2}}$ increases. This is entirely consistent with the progression from fast bubbles for small particles (small j_{CD}) to slow bubbles for larger particles.

For further details on bubbles in fluidized beds the reader is referred to the extensive literature including the books of Zenz and Othmer (1960), Cheremisinoff and Cheremisinoff (1984), Davidson *et al.* (1985) and Gibilaro (2001).

7.5 LIMITS ON SEPARATED FLOW

We now leave disperse flow limits and turn to the mechanisms that limit separated flow regimes.

7.5.1 Kelvin-Helmoltz instability

Separated flow regimes such as stratified horizontal flow or vertical annular flow can become unstable when waves form on the interface between the two fluid streams (subscripts 1 and 2). As indicated in figure 7.20, the densities of the fluids will be denoted by ρ_1 and ρ_2 and the velocities by u_1 and u_2. If these waves continue to grow in amplitude they will cause a transition to another flow regime, typically one with greater intermittency and involving plugs or slugs. Therefore, in order to determine this particular boundary of the separated flow regime, it is necessary to investigate the potential growth of the interfacial waves, whose wavelength will be denoted by λ (wavenumber, $\kappa = 2\pi/\lambda$). Studies of such waves have a long history originating with the work of Kelvin and Helmholtz and the phenomena they revealed have come to be called Kelvin-Helmholtz instabilities (see, for example, Yih 1965). In general this class of instabilities involves the interplay between at least two of the following three types of forces:

- a buoyancy force due to gravity and proportional to the difference in the densities of the two fluids. This can be characterized by $g\ell^3\Delta\rho$ where $\Delta\rho = \rho_1 - \rho_2$, g is the acceleration due to gravity and ℓ is a typical dimension of the waves. This force may be stabilizing or destabilizing depending on the orientation of gravity, g, relative to the two fluid streams. In a horizontal flow in which the upper fluid is lighter than the lower fluid the force is stabilizing. When the reverse is true the buoyancy force is destabilizing and this causes Rayleigh-Taylor instabilities. When the streams are vertical as in vertical annular flow the role played by the buoyancy force is less clear.
- a surface tension force characterized by $S\ell$ that is always stabilizing.
- a Bernoulli effect that implies a change in the pressure acting on the interface caused by a change in velocity resulting from the displacement, a of that surface. For example, if the upward displacement of the point A in figure 7.21 were to cause an increase in the local velocity of fluid 1 and a decrease in the local velocity of fluid 2, this would imply an induced pressure difference at the point A that would

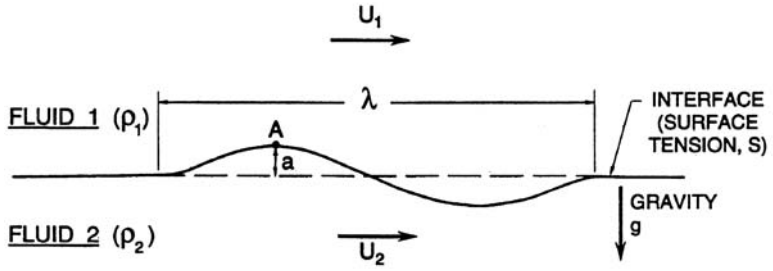

Figure 7.20. Sketch showing the notation for Kelvin-Helmholtz instability.

increase the amplitude of the distortion, a. Such Bernoulli forces depend on the difference in the velocity of the two streams, $\Delta u = u_1 - u_2$, and are characterized by $\rho(\Delta u)^2 \ell^2$ where ρ and ℓ are a characteristic density and dimension of the flow.

The interplay between these forces is most readily illustrated by a simple example. Neglecting viscous effects, one can readily construct the planar, incompressible potential flow solution for two semi-infinite horizontal streams separated by a plane horizontal interface (as in figure 7.20) on which small amplitude waves have formed. Then it is readily shown (Lamb 1879, Yih 1965) that Kelvin-Helmholtz instability will occur when

$$\frac{g\Delta\rho}{\kappa} + S\kappa - \frac{\rho_1\rho_2(\Delta u)^2}{\rho_1 + \rho_2} < 0 \tag{7.21}$$

The contributions from the three previously mentioned forces are self-evident. Note that the surface tension effect is stabilizing since that term is always positive, the buoyancy effect may be stabilizing or destabilizing depending on the sign of $\Delta\rho$ and the Bernoulli effect is always destabilizing. Clearly, one subset of this class of Kelvin-Helmholtz instabilities are the Rayleigh-Taylor instabilities that occur in the absence of flow ($\Delta u = 0$) when $\Delta\rho$ is negative. In that static case, the above relation shows that the interface is unstable to all wave numbers less than the critical value, $\kappa = \kappa_c$, where

$$\kappa_c = \left(\frac{g(-\Delta\rho)}{S}\right)^{\frac{1}{2}} \tag{7.22}$$

In the next two sections we shall focus on the instabilities induced by the destabilizing Bernoulli effect for these can often cause instability of a separated flow regime.

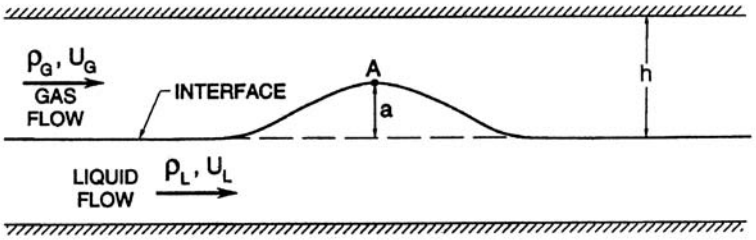

Figure 7.21. Sketch showing the notation for stratified flow instability.

7.5.2 Stratified flow instability

As a first example, consider the stability of the horizontal stratified flow depicted in figure 7.21 where the destabilizing Bernoulli effect is primarily opposed by a stabilizing buoyancy force. An approximate instability condition is readily derived by observing that the formation of a wave (such as that depicted in figure 7.21) will lead to a reduced pressure, p_A, in the gas in the orifice formed by that wave. The reduction below the mean gas pressure, $\bar{p}_G$, will be given by Bernoulli's equation as

$$p_A - \bar{p}_G = -\rho_G u_G^2 a/h \tag{7.23}$$

provided $a \ll h$. The restraining pressure is given by the buoyancy effect of the elevated interface, namely $(\rho_L - \rho_G)ga$. It follows that the flow will become unstable when

$$u_G^2 > gh\Delta\rho/\rho_G \tag{7.24}$$

In this case the liquid velocity has been neglected since it is normally small compared with the gas velocity. Consequently, the instability criterion provides an upper limit on the gas velocity that is, in effect, the velocity difference. Taitel and Dukler (1976) compared this prediction for the boundary of the stratified flow regime in a horizontal pipe of diameter, d, with the experimental observations of Mandhane *et al.* (1974) and found substantial agreement. This can be demonstrated by observing that, from equation 7.24,

$$j_G = \alpha u_G = C(\alpha)\alpha(gd\Delta\rho/\rho_G)^{\frac{1}{2}} \tag{7.25}$$

where $C(\alpha) = (h/d)^{\frac{1}{2}}$ is some simple monotonically increasing function of α that depends on the pipe cross-section. For example, for the $2.5cm$ pipe of figure 7.3 the factor $(gd\Delta\rho/\rho_G)^{\frac{1}{2}}$ in equation 7.25 will have a value of approximately $15m/s$. As can be observed in figure 7.3, this is in close agreement with the value of j_G at which the flow at low j_L departs from the stratified regime and begins to become wavy and then annular. Moreover the factor $C(\alpha)\alpha$ should decrease as j_L increases and, in figure 7.3, the boundary between stratified flow and wavy flow also exhibits this decrease.

7.5.3 Annular flow instability

As a second example consider vertical annular flow that becomes unstable when the Bernoulli force overcomes the stabilizing surface tension force. From equation 7.21, this implies that disturbances with wavelengths greater

than a critical value, λ_c, will be unstable and that

$$\lambda_c = 2\pi S(\rho_1 + \rho_2)/\rho_1\rho_2(\Delta u)^2 \tag{7.26}$$

For a liquid stream and a gas stream (as is normally the case in annular flow) and with $\rho_L \ll \rho_G$ this becomes

$$\lambda_c = 2\pi S/\rho_G(\Delta u)^2 \tag{7.27}$$

Now consider the application of this criterion to the flow regime maps for vertical pipe flow included in figures 7.6 and 7.8. We examine the stability of a well-developed annular flow at high gas volume fraction where $\Delta u \approx j_G$. Then for a water/air mixture equation 7.27 predicts critical wavelengths of $0.4cm$ and $40cm$ for $j_G = 10m/s$ and $j_G = 1m/s$ respectively. In other words, at low values of j_G only larger wavelengths are unstable and this seems to be in accord with the break-up of the flow into large slugs. On the other hand at higher j_G flow rates, even quite small wavelengths are unstable and the liquid gets torn apart into the small droplets carried in the core gas flow.